Anatomy of a summertime convective event over the Arabian region

Article

Published Version

Open Access

It is advisable to refer to the publisher's version if you intend to cite from the work. See Guidance on citing.

To link to this article DOI: http://dx.doi.org/10.1175/MWR-D-22-0082.1

Publisher: American Meteorological Society

www.reading.ac.uk/centaur

CentAUR

Anatomy of a Summertime Convective Event over the Arabian Region

Deepak Gopalakrishnan[a,b] Sourav Taraphdar,[a,c] Olivier M. Pauluis,[a,d] Lulin Xue,[e,f]
R. S. Ajayamohan,[a] Noor Al Shamsi,[g] Sisi Chen,[f] Jared A. Lee,[f] Wojciech W. Grabowski,[f] Changhai Liu,[f]
Sarah A. Tessendorf,[f] and Roy M. Rasmussen[f]

[a] *Arabian Center for Climate and Environmental Sciences, New York University Abu Dhabi, Abu Dhabi, United Arab Emirates*
[b] *Central Michigan University, Mount Pleasant, Michigan*
[c] *Pacific Northwest National Laboratory, Richland, Washington*
[d] *Courant Institute of Mathematical Sciences, New York University, New York, New York*
[e] *Hua Xin Chuang Zhi Science and Technology LLC, Beijing, China*
[f] *Research Applications Laboratory, National Center for Atmospheric Research, Boulder, Colorado*
[g] *National Center of Meteorology, Abu Dhabi, United Arab Emirates*

ABSTRACT: This study investigates the structure and evolution of a summertime convective event that occurred on 14 July 2015 over the Arabian region. We use the WRF Model with 1-km horizontal grid spacing and test three PBL parameterizations: the Mellor–Yamada–Nakanishi–Niino (MYNN) scheme; the Asymmetrical Convective Model, version 2, (ACM2) scheme; and the quasi-normal scale-elimination (QNSE) scheme. Convection initiates near the Al Hajar Mountains of northern Oman at around 1100 local time (LT; 0700 UTC) and propagates northwestward. A nonorographic convective band along the west coast of the United Arab Emirates (UAE) develops after 1500 LT as a result of the convergence of cold pools with the sea breeze from the Arabian Gulf. The model simulation employing the QNSE scheme simulates the convection initiation and propagation well. Although the MYNN and ACM2 simulations show convective initiation near the Al Hajar Mountains, they fail to simulate the development of the convective band along the UAE west coast. The MYNN run simulates colder near-surface temperatures and a weaker sea breeze, whereas the ACM2 run simulates a stronger sea breeze but a drier lower troposphere. Sensitivity simulations using horizontal grid spacings of 9 and 3 km show that lower-resolution runs develop broader convective structures and weaker cold pools and horizontal wind divergence, affecting the development of convection along the west coast of the UAE. The 1-km run using the QNSE PBL scheme realistically captures the sequence of events that leads to the moist convection over the UAE and adjacent mountains.

KEYWORDS: Deep convection; Orographic effects; Precipitation; Sea breezes; Isentropic analysis; Cloud-resolving models

1. Introduction

The Arabian Peninsula, including the United Arab Emirates (UAE), is characterized by a hyperarid climate. The observed rainfall shows a spatially distinct pattern, with the eastern part of the UAE receiving an average rainfall of approximately 130 mm and the southern desert of the UAE typically recording approximately 20 mm yr^{-1} (Ouarda et al. 2014; Schwitalla et al. 2020; Francis et al. 2021). These estimates may vary because global precipitation products exhibit considerable variability in the rainfall estimates over the UAE region (Wehbe et al. 2017). Although the annual rainfall is relatively low, the observed pattern shows clear seasonal asymmetry. Almost 80% of the annual rainfall of the UAE is received during

the winter season, whereas summertime convective events contribute approximately 20% (Wehbe et al. 2017; Steinhoff et al. 2018; Schwitalla et al. 2020). The wintertime rainfall events are generally associated with the intrusion of midlatitude weather systems, including extratropical cyclones from the Mediterranean region (Wehbe et al. 2019; Wehbe and Temimi 2021; Taraphdar et al. 2021). However, summertime convective events in the UAE generally develop through a three-way convergence of the sea breezes from the Gulf of Oman (refer to Figs. 1a and 2b for local geography) and the Arabian Gulf with the Arabian heat low flow (Steinhoff et al. 2018; Wehbe et al. 2021). The surface heat low over the Arabian Peninsula is a persistent feature during the boreal summer (Ackerman and Cox 1982; Smith 1986), showing considerable diurnal variability with an intensification in the afternoon hours (Fonseca et al. 2022). The location and strength of the heat low can significantly alter the pattern of convergence in the lower troposphere and the moisture inflow, and thereby modulate the occurrence of convective activity over the region.

Orographically forced convective events are very common during summer near the Al Hajar Mountains. Branch et al. (2020) analyzed the summertime convective initiation (CI) over the Al Hajar Mountains using *Meteosat-7* data during the period 2010–16 and observed that approximately 55 convective events occur in a typical summer. The CI generally
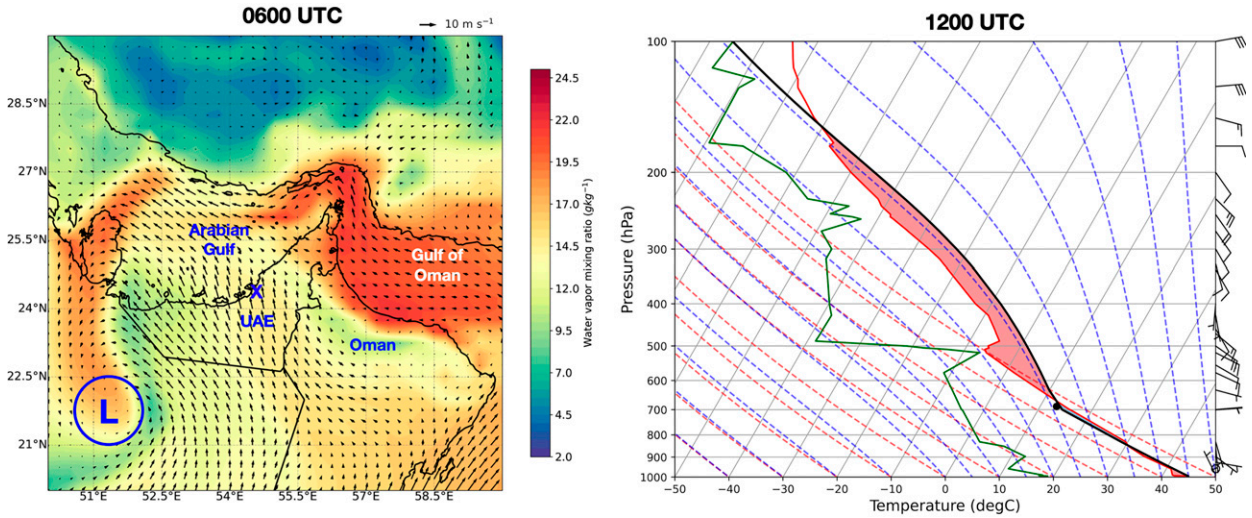
FIG. 1. (a) The 975-hPa water vapor mixing ratio (shaded; g kg^{-1}) and wind field (vectors; m s^{-1}) from ERA5 valid at 0600 UTC 14 Jul 2015. The blue "x" indicates the location of Abu Dhabi airport. The location of the heat low is marked with a blue circled "L." (b) The skew T–log$p$ plot of the radiosonde observation from the Abu Dhabi airport at 1200 UTC 14 Jul 2015. The red line denotes the air temperature profile, and the green line indicates the dewpoint temperature profile. The red shading and the blue shading (thin sliver above the black line near the black dot) represent surface-based CAPE and CIN, respectively.

begins over higher terrain during the day and then propagates northward and westward. The secondary development of convective cells west of the mountains is generally associated with the convergence of cold pools from the primary convective cells with the Arabian Gulf sea breeze and the Arabian heat low flow. The nonorographic rainfall events along the western coast of the UAE are primarily attributed to the convergence of the southerly branch of the Arabian heat low flow with the sea breeze from the Arabian Gulf (Steinhoff et al. 2018). Steinhoff et al. (2018) noted the formation of a secondary circulation over the eastern parts of the UAE in the morning hours due to a three-way convergence of the sea breeze from the Gulf of Oman, Arabian Gulf, and the inflow associated with the Arabian heat low. Development of this secondary circulation is crucial as it provides favorable conditions for the development of deep convection by preventing the intrusion of dry air from land. Other factors that promote CI over the arid, mountainous regions include a strong surface temperature gradient and the presence of an upper or midlevel trough (Knippertz et al. 2009; Francis et al. 2019).

Being a hyperarid region, the UAE and adjoining areas face severe water scarcity (Murad et al. 2007; Odhiambo 2017). In addition, water demand is increasing due to the growing population and ongoing industrial and agricultural activities (Branch et al. 2020). Hence, rainfall is crucial in maintaining groundwater and recharging underground aquifers (Bruintjes and Yates 2003; Murad et al. 2007; Wehbe et al. 2018). To resolve this crisis, there have been several weather
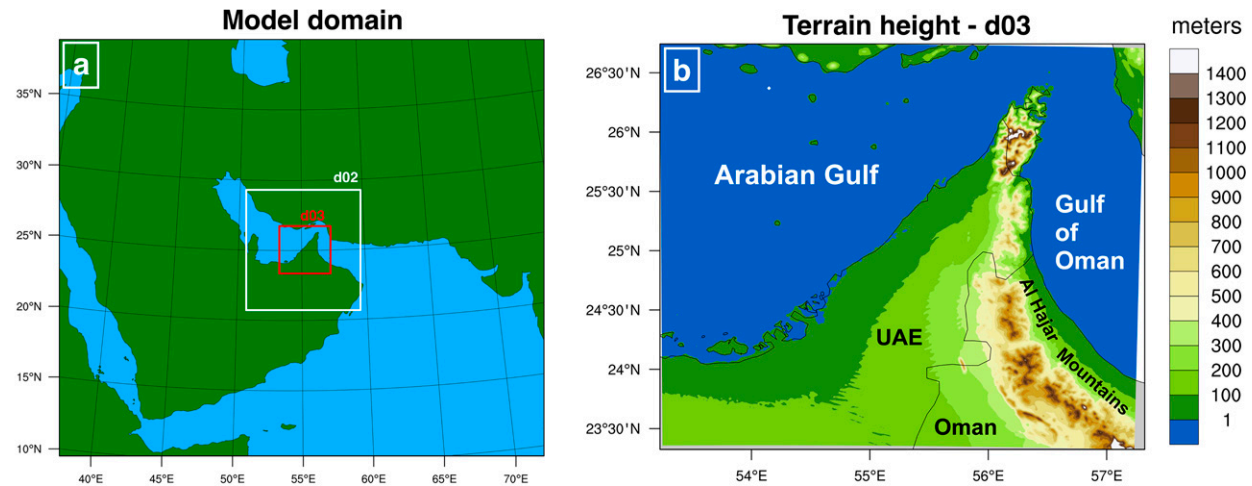

FIG. 2. (a) The WRF Model domains, and (b) terrain height (m) for the innermost domain.

modification attempts in the UAE, primarily focusing on increasing rainfall through cloud seeding (Al Hosari et al. 2021). The UAE Research Program for Rain Enhancement Science (UAEREP) is a dedicated program for improving scientific knowledge of rain-enhancing procedures. The results from seeding experiments indicate an average increase of 23% in annual surface rainfall over the target areas in the UAE (Al Hosari et al. 2021). One of the major challenges in successful cloud seeding is identifying the development of convective clouds in advance. Thus, accurate numerical simulation of summertime convection is of utmost importance.

Schwitalla et al. (2020) analyzed the simulation of a summertime convective event that occurred on 14 July 2015 using the WRF Model, examining the impact of various PBL and microphysics parameterization schemes while using a convection-permitting horizontal grid spacing (2.7 km). The above study used the Mellor–Yamada–Nakanishi–Niño (MYNN) scheme and the Yonsei University (YSU) scheme for the PBL parameterization and the Thompson–Eidhammer aerosol-aware scheme, the Thompson 2-moment scheme, and the WRF double-moment 6-class (WDM6) scheme for the microphysics parameterization. The results showed that the combination of the MYNN PBL scheme and the Thompson–Eidhammer microphysics scheme yielded the best result. Although the simulation using this configuration produced more CAPE, it suffered from insufficient cloud liquid water and therefore failed to reproduce the observed rainfall pattern accurately. In particular, the WDM6 scheme significantly underestimated the liquid water within the clouds.

In a recent study, Francis et al. (2021) investigated the simulation of another summertime convective event that occurred on 5 September 2017 with the WRF Model. Francis et al. (2021) employed a model configuration using four nested domains, with the innermost domain having a horizontal grid spacing of 0.833 km. That study utilized four different forcing datasets for the WRF simulations: the Global Forecast System (GFS), Climate Forecast System Reanalysis (CFSR), European Centre for Medium-Range Weather Forecasts ERA-Interim, and ERA5. Similar to Schwitalla et al. (2020), Francis et al. (2021) also used the MYNN level-2.5 PBL scheme and the Thompson–Eidhammer aerosol-aware microphysics scheme. The authors observed that the fourth domain of subkilometer grid spacing did not provide significant added value. A comparison with the observations from a microwave radiometer installed over the mountains indicated that the WRF simulations failed to capture the presence of the mesoscale convective systems appropriately. Francis et al. (2021) noted that among the four simulations, the one forced with the GFS fields showed a marginally better skill in simulating the convective event, while the simulation using the ERA-Interim fields showed the least skill. The above study highlighted that an accurate simulation of the observed cloud and precipitation patterns is extremely challenging over the UAE region. The authors attributed the unsuccessful simulation of the mesoscale convective system to the misrepresentation of the soil moisture fields over the UAE region.

The studies mentioned above (i.e., Schwitalla et al. 2020; Francis et al. 2021) suggest that realistic simulation of cloud and rainfall patterns associated with summertime convective systems over the UAE region is extremely challenging. Moreover, studies that examine the skill of NWP models in simulating summertime precipitation events over the UAE and adjacent mountainous regions are quite limited. Therefore, a study demonstrating the realistic simulation of a summertime precipitation event and the underlying mechanisms leading to deep convection near the UAE and the adjacent Al Hajar Mountains fills a gap in the literature. Additionally, a skillful NWP model configuration can provide significant added value to the ongoing cloud-enhancement experiments in the UAE region.

In this study, we conduct a set of cloud-resolving scale (with 1-km horizontal grid spacing) numerical simulations using the WRF Model to simulate a summertime convective event and the mechanisms that lead to deep convection. We choose the event considered by Schwitalla et al. (2020) in their study. We also aim to examine the sensitivity of the WRF Model simulations to three different PBL schemes and investigate how changes in horizontal grid spacing affect convection and precipitation. Section 2 provides a brief description of the convective event considered in the study. Section 3 outlines the details of the model and experimental design. We discuss the results from the model simulation in section 4. Section 5 provides the summary and conclusions.

2. Case description

Summertime convective events over the eastern side of the Al Hajar Mountains often develop due to the orographic lifting of warm moist air from the Gulf of Oman and are most common in July (Branch et al. 2020). In this study, we consider a typical summertime convective rainfall that occurred on 14 July 2015. Figure 1a indicates the presence of sufficiently moist air with mixing ratio values as high as 22 g kg^{-1} off the east coast of UAE at 0600 UTC (1000 LT). The sea breeze advects moisture-rich air from the Gulf of Oman into the Al Hajar Mountains, providing favorable conditions for CI over the mountains. The radiosonde observation at 1200 UTC 14 July 2015 from the Abu Dhabi airport indicates a surface-based CAPE of 1842 J kg^{-1}. The lifting condensation level (LCL) is at 688 hPa, with the level of free convection and equilibrium level at 661 and 155 hPa, respectively. The high LCL suggests that the lower atmosphere is very dry. The temperature profile shows an inversion with a magnitude of 4 K and the dewpoint profile implies strong and sharp drying at 500 hPa (Fig. 1b). Although the Abu Dhabi airport is located away from the location of rainfall, this sounding is representative of the thermodynamic profile of the region.

3. Experimental and analysis methods

a. Model domain and configuration

We use the WRF Model, version 4.1.2 (Skamarock et al. 2019), to conduct the numerical experiments. We configured the WRF Model with three nested domains and two-way nesting with a horizontal grid spacing of 9, 3, and 1 km as shown in Fig. 2. The outer 9-km domain covers the entire Middle

East region together with most of the Red Sea and the Arabian Sea to capture the large-scale features. The domain with 3-km horizontal grid spacing covers the Gulf of Oman and much of the Arabian Gulf to capture the moisture transport toward the UAE region. The innermost domain with 1-km horizontal grid spacing aims to accurately simulate the CI and subsequent precipitation over the UAE region. This high-resolution domain can also better resolve the sea breezes from the Arabian Gulf and the Gulf of Oman. All three domains have 45 terrain-following vertical levels up to the 20-hPa model top.

The cumulus parameterization is turned off for all domains, meaning that convection is explicitly resolved in all simulations. Although 9-km grid spacing (gray-zone resolution) cannot fully resolve each convective cloud, studies show that the gray-zone simulations can capture the general features of convective clouds and their interaction with the large-scale environment fairly well (Pauluis and Garner 2006; Chen et al. 2018; Jing et al. 2020; Taraphdar et al. 2021). The simulations use the Thompson–Eidhammer aerosol-aware microphysics scheme (Thompson and Eidhammer 2014). That scheme has six classes of hydrometeors and employs a double-moment representation for rain and cloud ice. More important, this particular scheme can incorporate the effect of aerosols such as cloud condensation and ice nuclei. Accordingly, this scheme includes two prognostic variables to account for hygroscopic ("water friendly") aerosols and nonhygroscopic ("ice friendly") aerosols. Recent studies (Francis et al. 2021; Taraphdar et al. 2021) have shown that the Thompson–Eidhammer scheme provides a better simulation of rainfall over the Arabian region. Furthermore, this scheme may be particularly useful for cloud-seeding applications.

We use three different PBL schemes to represent boundary layer processes: the quasi-normal scale-elimination (QNSE) scheme, Mellor–Yamada–Nakanishi–Niño (MYNN) level-3 scheme, and Asymmetrical Convective Model, version 2, (ACM2) scheme. QNSE (Sukoriansky et al. 2005) and MYNN (Nakanishi and Niino 2006, 2009) are local closure schemes that use the turbulent kinetic energy (TKE) as a prognostic variable while the ACM2 (Pleim 2007a,b) scheme is a nonlocal, first-order closure scheme that follows nonlocal vertical mixing and local downward mixing. The model simulations use the QNSE, MYNN, and Pleim–Xu surface layer schemes for the QNSE, MYNN, and ACM2 PBL parameterization schemes, respectively. We use the Noah land surface model (LSM) with multiphysics (NOAH-MP) scheme with an explicit vegetation canopy to represent land surface processes (Niu et al. 2011). Weston et al. (2019) examined the performance of the Noah LSM and the updated Noah-MP LSM over the UAE region and reported a better simulation of near-surface temperature and relative humidity, leading to a more realistic simulation of the sea breeze in the WRF Model using NOAH-MP. The present configuration uses RRTMG to parameterize longwave and shortwave radiative processes (Iacono et al. 2008) and it employs the correlated-k approach to compute the fluxes and heating rate. The physics schemes used in the present study are summarized in Table 1.

TABLE 1. Summary of the physics packages utilized in this study.

Model physics	Scheme used
Microphysics	Thompson–Eidhammer aerosol-aware
PBL	QNSE, MYNN, and ACM2
Cumulus	None
Radiation (longwave and shortwave)	RRTMG
Land surface	Noah-MP
Surface layer	QNSE, MYNN, and Pleim–Xiu

Francis et al. (2021) noted that it is very important to accurately initialize soil moisture for a better rainfall simulation. This study uses an updated version of land use/land cover (LULC) and soil texture data for the UAE region. The LULC dataset was prepared after a dedicated field campaign performed as part of the UAEREP. The UAE National Center of Meteorology (NCM) developed the soil texture data based on a comprehensive field survey (Aldababseh et al. 2018). More details on the updates in the LULC and soil texture dataset can be found in Temimi et al. (2020).

b. Simulation design

We conducted three numerical simulations corresponding to the three PBL schemes with the above-described configurations for 36 h, starting at 1200 UTC 13 July 2015. The initial and lateral boundary conditions are derived from ERA5 fields, which are available at a horizontal grid spacing of 0.25° with 1-h temporal resolution (Hersbach et al. 2020). The model integration time step is 30 s for the 9-km outer domain, 10 s for the 3-km domain, and 3.333 s for the 1-km innermost domain. The first 12 h of each simulation are discarded as spinup. Gridded output from all three model domains is stored at 15-min intervals.

4. Results from the 1-km run

a. Rainfall pattern

Accurate simulations of precipitation are of primary interest to cloud-seeding experiments. We, therefore, compare the model-simulated rainfall with the radar-derived rainfall estimate to examine the skill of the WRF Model in reproducing the observed rainfall pattern. The radar rainfall estimate is prepared by NCM combining observations from four weather radars, which operate at the C band. More details on the preparation of the merged rainfall estimate are available in Wehbe et al. (2020). The radar rainfall estimate (Fig. 3a) depicts three loosely connected orographic rainfall bands over the mountains and another band parallel to but inland of the west coast of the UAE. The model runs show considerable overestimation in the rainfall amounts relative to the radar estimate. These differences could be partly due to the uncertainties in the radar observations, as terrain blockage and merging uncertainties can impact radar-derived precipitation estimates over complex terrain (Wehbe et al. 2020). Moreover, the model-simulated rainfall is the direct accumulation of rainfall
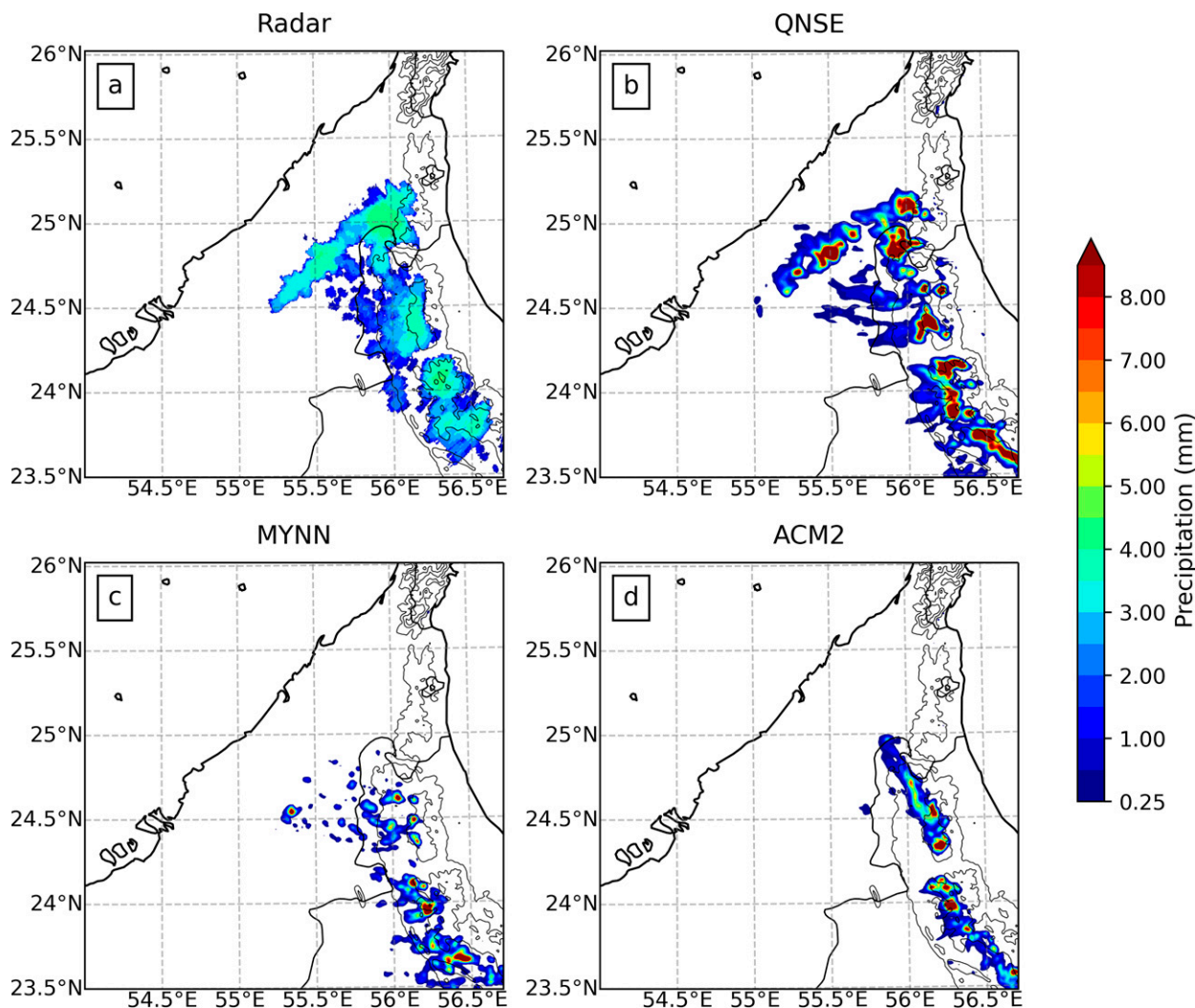
FIG. 3. The 24-h accumulated rainfall, valid at 0000 UTC 15 Jul 2015 from the (a) radar-derived estimates and (b) QNSE, (c) MYNN, and (d) ACM2 WRF simulations. The thin black contours indicate terrain height from 400 to 1200 m at 300-m intervals. The model-derived rainfall in (b)–(d) is from the 1-km domain.

at each time step, while the radar rainfall estimate is prepared after several postprocessing steps.

The QNSE run simulates the observed rainfall pattern very well, whereas the other two runs fail to reproduce the rainfall bands appropriately. In particular, the development of the non-orographic precipitation band is completely missing in both MYNN and ACM2 runs. The model simulations, in general, show pulse-type rainfall maxima at different spots along the mountain range. The QNSE run shows a better-organized rainfall structure than the other two WRF simulations. The ACM2 run also produces the orographic rainfall bands to a reasonable extent, whereas the MYNN run produces more scattered convection. Neither the MYNN nor ACM2 simulations show the nonorographic rainfall maximum centered at 25°N, 56°E (Fig. 3a). Therefore, it appears that the QNSE PBL scheme has a positive impact on accurately reproducing the rainfall pattern over the UAE region. A recent study by Taraphdar et al. (2021) also

reported that the QNSE PBL scheme provides more accurate simulations of rainfall in winter over the UAE region than the ACM2 or MYNN schemes. The near-surface air is warmer and moister in the QNSE simulation, yielding enhanced moisture flux convergence and more CAPE than in the ACM2 run. We explore the meteorological conditions in all three simulations in more detail in the forthcoming sections.

b. The observed and the simulated convection

Here we compare the observed radar reflectivity with the model-simulated reflectivity only from the QNSE run (Fig. 4) to understand how well the model reproduces the intensity of deep convection. CI near the Al Hajar Mountains begins at around 0615 UTC in the model simulation, whereas the NCM radar indicates CI at 0740 UTC, nearly 1.5 h later (not shown). At 0900 UTC, convection over the Al Hajar Mountains peaks with a column-maximum observed reflectivity of ~52 dBZ at 24.4°N,
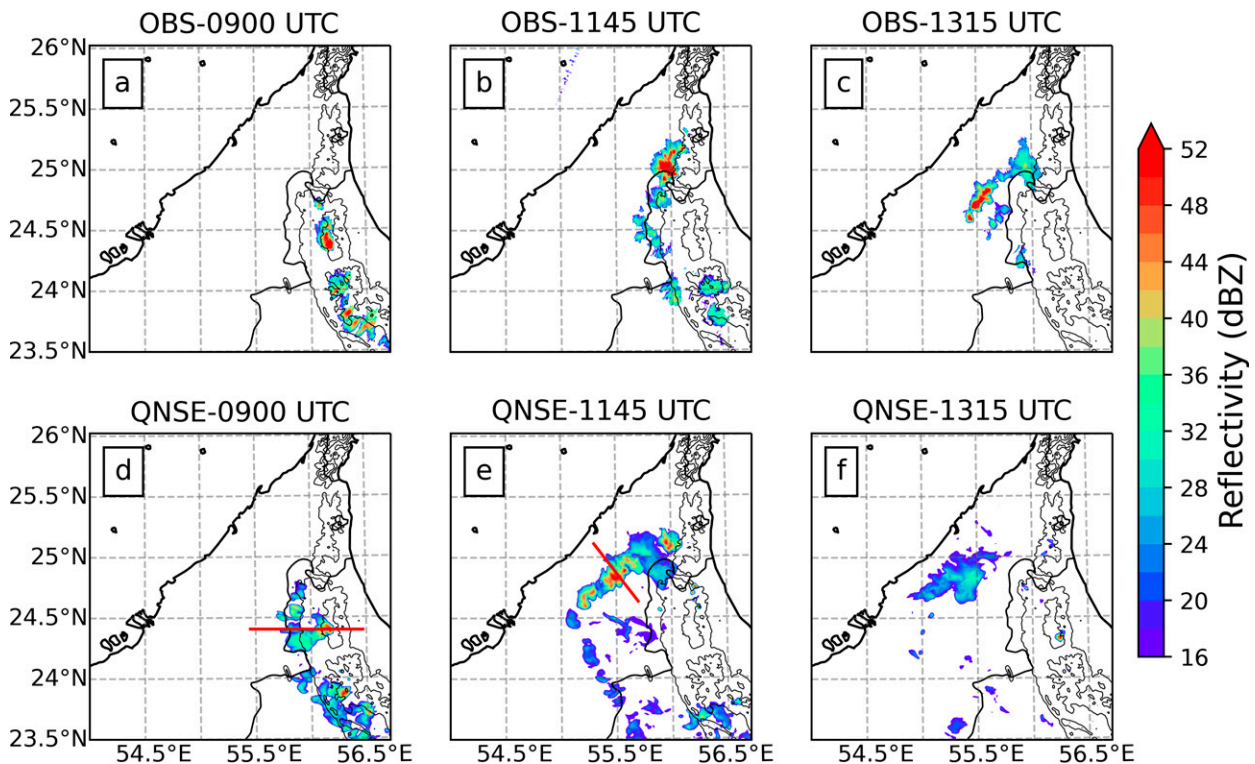
FIG. 4. Column-maximum radar reflectivity from (a)–(c) the NCM radar and (d)–(f) the QNSE simulation at (left) 0900 UTC, (center) 1145 UTC, and (right) 1315 UTC. The red lines indicate the cross sections in Fig. 5, below.

56.1°E (Fig. 4a). The QNSE run captures this band of convection and the location of the peak reflectivity very well (Fig. 4d). At 1145 UTC, there is another major peak in the observed reflectivity near 25°N, 56°E (Fig. 4b). Although the model simulates this convective maximum well (Fig. 4e), it produces convection over a larger area that extends even farther west than observed. Another band of convection inland from the west coast develops by 1315 UTC (Fig. 4c), although it is a little farther inland and later than in the model simulation, where it is already dissipating at this time (Fig. 4f). Recalling that the modeled convection leads the observed convection by approximately 1.5 h, we conclude that the QNSE simulation is able to reproduce the sequence of events realistically, despite the timing and location differences.

An examination of vertical cross sections can illustrate orographically forced moist convection, the collision of the sea breeze from the Gulf of Oman with the mean flow over the land, and the convergence of cold pools with the sea breeze from the Arabian Gulf. These diagnostics provide a better understanding of the underlying mechanisms that lead to deep convection over the region. Figure 5 shows the longitude–height cross section of WRF-simulated convection from the QNSE run in terms of equivalent potential temperature θ_e and vertical circulation ($u \times w$). Figure 5a depicts the vertical structure of the deep convection near the Al Hajar Mountains at 24.4°N (refer to the red line in Fig. 4d that indicates the cross section) at 0730 and 0900 UTC. The time evolution of the convection in the mountainous region reveals that this convective cell initiates at approximately 0730 UTC as diurnal

thermally induced upslope westerly flow along the western mountain slope converges with the sea breeze from the Gulf of Oman (Fig. 5a). The sea breeze only extends to 1.5 km AGL. However, the moist convection reaches up to an altitude of 5 km MSL over the mountain peak. Figure 5b shows the mature phase of the same convective plume at 0900 UTC. There is a strong downdraft originating from around 4 km MSL, which promotes additional moist convection along the leading edge of the outflow. The deep convection extends above 8 km MSL, and the presence of high-θ_e air extends up to a height of 7 km MSL ($\theta_e \sim 362$ K).

Figures 5c and 5d illustrate the vertical structure of the nonorographic convective cells that develop parallel to the west coast of the UAE at 1100 and 1145 UTC. The cross section is perpendicular to the convective band, as indicated in Fig. 4e. High-θ_e air advected from the Arabian Gulf at 1100 UTC converges with the cold pool from the earlier convective cells, with new convection initiating at 55.59°E, extending up to 6 km MSL. Forty-five minutes later, Fig. 5d reveals a well-developed storm structure, with downdraft from 5 km MSL. Although the air from the Arabian Gulf exhibits significantly lower θ_e values ($\sim$355 K) than the air from the Gulf of Oman ($\sim$375 K), the lower to midtroposphere near the west coast of the UAE is more well-mixed in terms of θ_e.

c. The sea-breeze structure in the QNSE simulation

We examine the distribution of near-surface air temperature and winds to analyze the land-sea thermal contrast and the sea breezes because they modulate CI near the Al Hajar
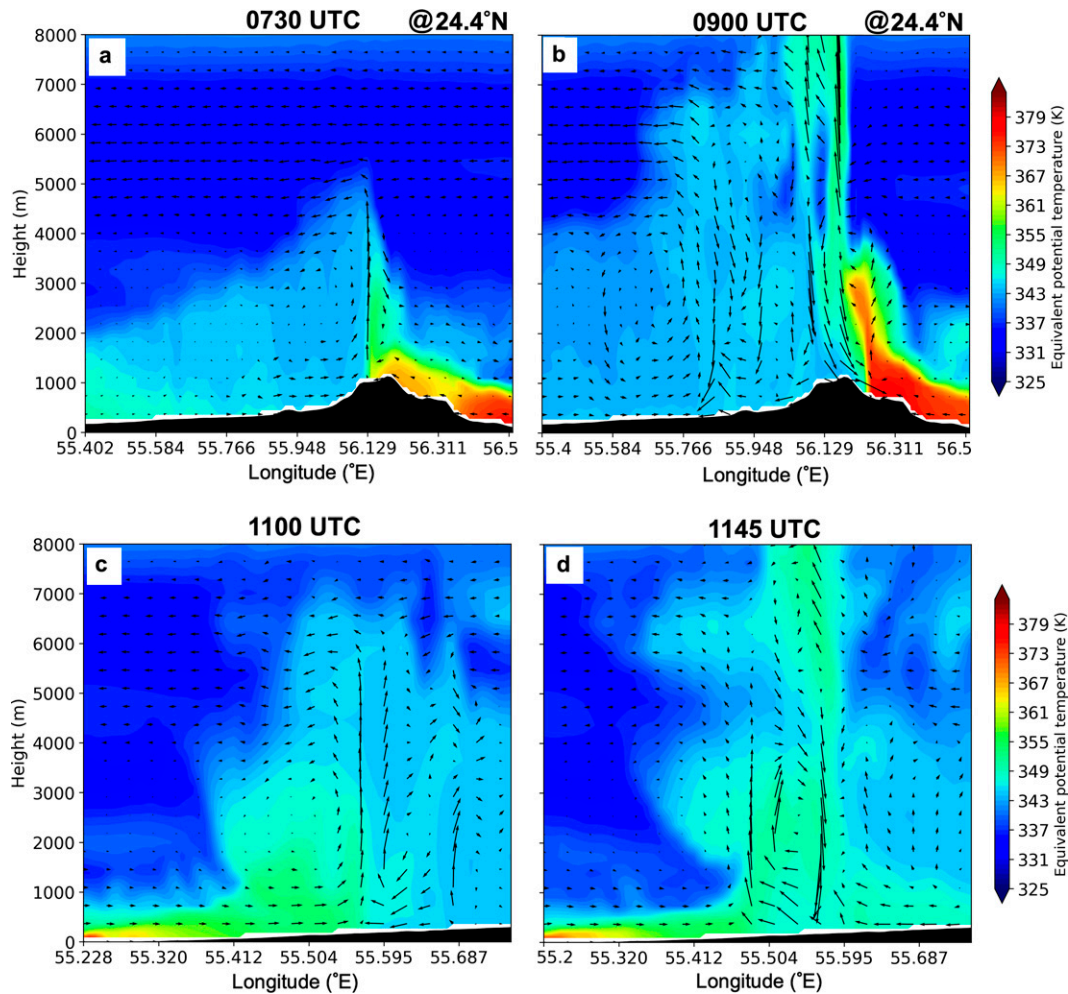
FIG. 5. Longitude–height cross sections of equivalent potential temperature (shaded; K) overlaid with the in-plane winds (vectors; m s^{-1}) along (top) 24.4°N and (bottom) 24.8°N at (a) 0730, (b) 0900, (c) 1100, and (d) 1145 UTC. The cross sections are defined in Figs. 4d and 4e. The vertical motions are scaled by a factor of 5.

Mountains. Figures 6a–c indicate that there is a strong land–sea temperature contrast, and the maximum surface heating occurs over the southwestern parts of the domain, near the coast. The 2-m temperature is generally 5°–10°C lower on the eastern side of the mountains. The surface temperature contrast between the mountains and the Gulf of Oman is still sufficient to generate a sea breeze on the eastern side of the Al Hajar Mountains. There is also surface convergence over the higher terrain between the sea breeze and southerly winds from the interior desert southwest of the mountains. Although the sea breeze from the Arabian Gulf is much weaker at 0800 UTC, it becomes stronger by 1000 and 1200 UTC. The simulation indicates the presence of cold pools and associated diverging winds over the mountains at 1000 UTC (marked with a blue circle, Fig. 6b), resulting from convective outflows. There are two additional cold pools just inland of the west coast of the UAE at 1200 UTC. The diverging winds from these cold pools are encountering the sea breeze from the Arabian Gulf (marked with a magenta ellipse in Fig. 6c),

yielding convergence that may trigger further development of moist convection, as discussed further below.

We analyze the moisture distribution at 975 hPa (Figs. 6d–f) to investigate the moisture advection associated with the sea breeze from the Gulf of Oman and the Arabian Gulf. The air on the eastern side of the mountains is moist, with water vapor mixing ratios generally ranging from 18 to 23 g kg^{-1} over land. The wind speed is also high (~10 m s^{-1}) on the eastern side of the Al Hajar Mountains, leading to strong moisture advection from the Gulf of Oman. The northwest coast of the UAE is drier with strong dry-air advection from the desert farther south (Figs. 6e–f). Nevertheless, the sea breeze from the Arabian Gulf transports moderate moisture to the western UAE (up to ~17 g kg^{-1} at 1000 UTC).

The time evolution of precipitable water (Figs. 6g–i) also confirms the sequence of events described above. Precipitable water increases along the east coast of the UAE at 0800 UTC and especially to the east of a cold pool over the mountain ridge (near 24.5°N, 56°E) at 1000 UTC (Fig. 6h). This local
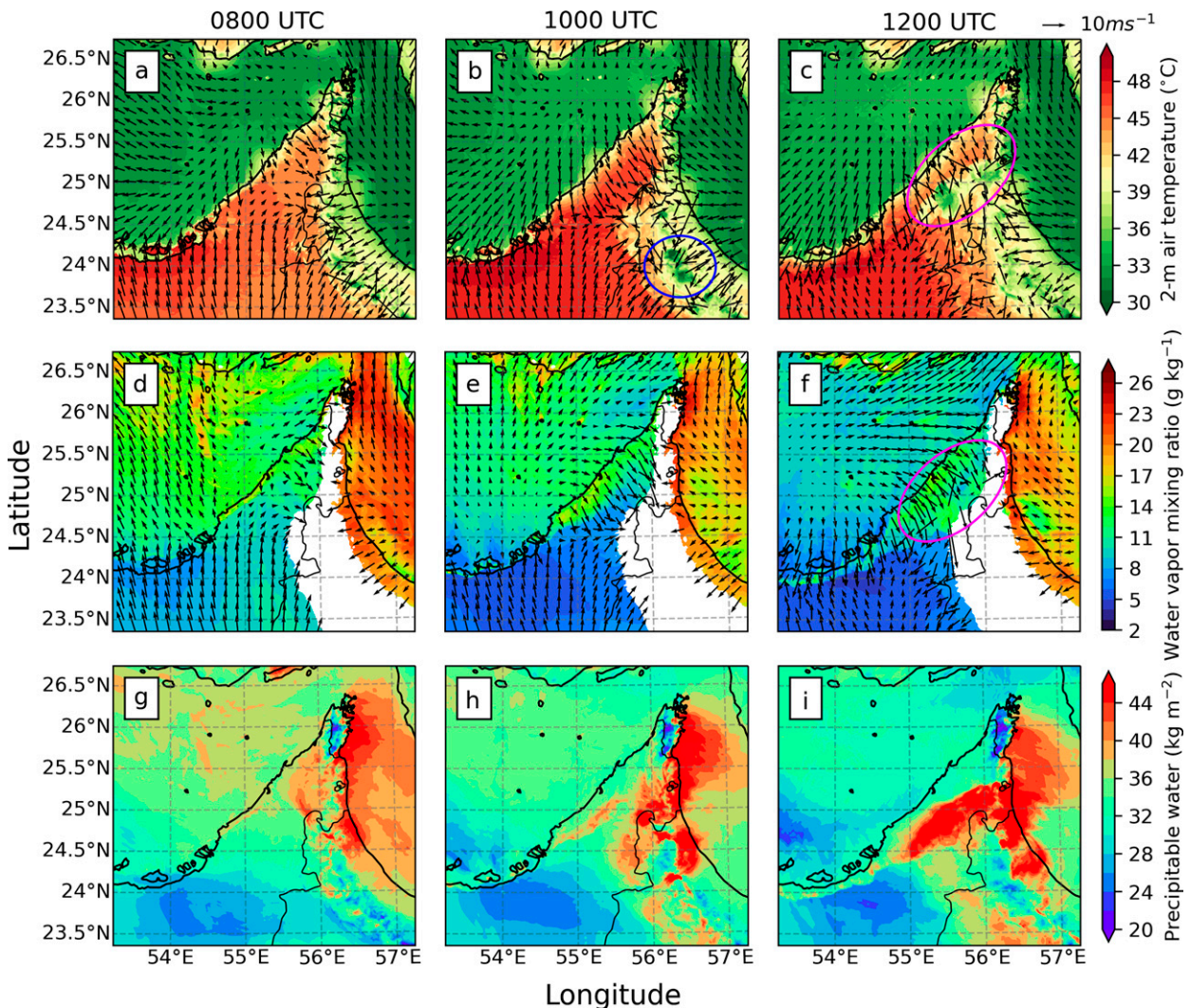
FIG. 6. WRF modeled (a)–(c) 2-m air temperature (shaded; °C) and 10-m wind vectors, (d)–(f) 975-hPa water vapor mixing ratio (shaded; g kg^{-1}) and wind vectors, and (g)–(i) precipitable water (shaded; kg m^{-2}) valid at (left) 0800, (center) 1000, and (right) 1200 UTC 14 Jul 2015 from the QNSE run. The cold pools are located inside the blue circle in (b) and the magenta ellipses in (c) and (f).

maximum in precipitable water is likely the result of the vertical advection of moisture due to the convergence of the propagating cold pool and the sea breeze from the Gulf of Oman. Moreover, deep convection transports a significant amount of moisture upward, leading to the buildup of precipitable water. Even more striking is the similar buildup of precipitable water near the west coast of the UAE.

d. Cold pools and their convergence with the sea breeze

To visualize how cold pools initiate the development of secondary convection, primarily over the west coast of the UAE, we examine the near-surface wind divergence and 2-m air temperature (Fig. 7). At 0930 and 1000 UTC, there are cold pools, which have been discussed briefly in section 4c (refer to the discussion on Fig. 6c). The cold pools encounter (i) the sea breeze from the Gulf of Oman to their northeast and (ii) flow from the inland region to their southwest (Figs. 7a,b). The convergence at the

eastern and western boundaries of the outflow is stronger at 0930 UTC than at 1000 UTC. The lower row of Fig. 7 demonstrates the convergence of a larger cold pool primarily with the sea breeze from the Arabian Gulf. The snapshots at 1100 and 1130 UTC indicate very high values of wind divergence (>0.005 s^{-1}) at several locations near the west coast. The 2-m air temperature within the cold pools is about 8°C less than the surroundings. The leading edge of the diverging winds collides with the sea breeze from the Arabian Gulf, forming a strong band of convergence parallel to the west coast of the UAE. This band of convergence strengthens further over the next 30 min, as seen in Fig. 7d.

e. The sea breezes and cold pools in MYNN and ACM2 simulations

It has been noted in section 4a that the MYNN and ACM2 runs fail to reproduce the precipitation distribution realistically.
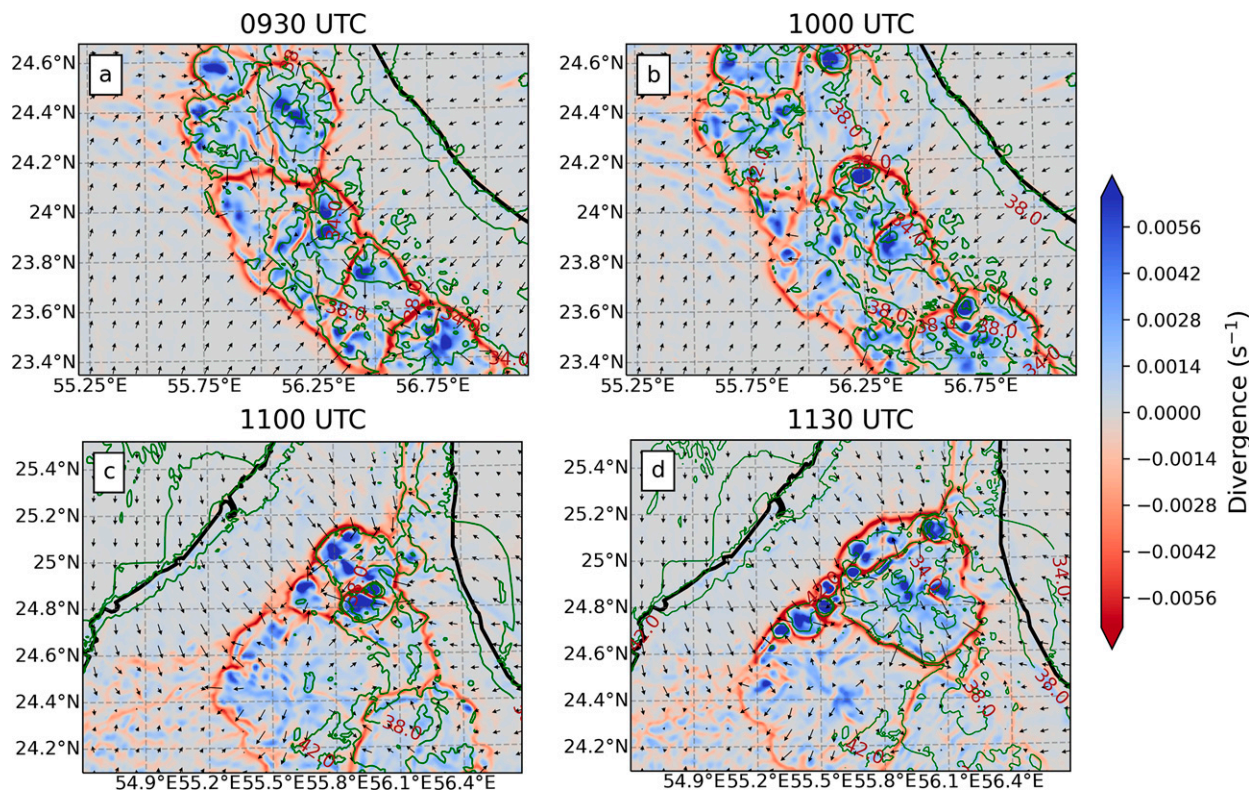
FIG. 7. Divergence of 10-m horizontal wind (shaded; s^{-1}) and horizontal wind (vectors) overlaid with 2-m temperature (green contours; °C) at (a) 0930, (b) 1000, (c) 1100, and (d) 1130 UTC. The top and bottom rows depict cold pools at different locations, respectively. Thick black lines mark the coastline.

The results from previous sections reveal that the sea breeze from the Gulf of Oman and the Arabian Gulf and their convergence with the cold pools are the major factors that modulate precipitation over the region. Therefore, it is important to examine how well the MYNN and ACM2 runs capture the sea breeze and moisture distribution.

Figure 8 clearly indicates a strong land–sea temperature contrast. Both simulations capture the broader features such as strong daytime heating and the sea breezes from both Gulfs. However, the MYNN run (top row) produces relatively cooler surface temperatures and weaker sea breezes than the ACM2 run. For instance, the 2-m air temperature in the proximity of the Al Hajar Mountains in the MYNN simulation is 2°–3°C lower than in the ACM2 run. This difference in temperature also reduces the strength of the sea breeze in the MYNN simulation. Furthermore, the 10-m winds over interior eastern UAE and western Oman weaken considerably with time, and by 1200 UTC, they nearly diminish completely. The sea breeze from the Arabian Gulf is also weaker in the MYNN run. A comparison of the 2-m temperature and sea breeze distributions from these two simulations with the corresponding fields from the QNSE run (Figs. 6a–c) reveals that the QNSE run simulates a much stronger sea breeze from both the Gulf of Oman and Arabian Gulf. In addition, the wind field over the land is also notably stronger in the QNSE simulation.

It is readily apparent from Fig. 9 that the ACM2 run simulates significantly drier air over land, and marginally drier air over the Arabian Gulf, while the air over the Gulf of Oman has a similar moisture content to that in the MYNN simulation. The ACM2 run transports drier air from the interior desert that converges with the moist air advecting from the Arabian Gulf, and this, in turn, leads to substantial mixing. At 1000 and 1200 UTC, the east coast of Oman exhibits notably lower mixing ratios than those in the MYNN simulation. Although the moisture content is higher on the coasts in the MYNN run, the winds are not strong enough to transport this moisture into the mountains to sustain deep convection. On the west coast of the UAE, the MYNN run shows significant advection of moisture due to the sea breeze. However, the mean wind strength over the land is very weak, and therefore, convergence and moist convection are almost absent near the west coast. A comparison with Figs. 6d–f indeed suggests that the QNSE run better simulates the sea breeze and the moisture field. Particularly, the southwesterly wind field over the inland desert (just west of the Al Hajar Mountains) supports stronger convergence with the moist air from the Gulf of Oman. The eastern side of the mountain range exhibits higher mixing ratios in the QNSE simulation. For instance, along the Oman coast, the QNSE run shows a water vapor mixing ratio as high as 23 g kg^{-1} at 0800 UTC (Fig. 6a), which is approximately 2–3 g kg^{-1} higher than in the other two simulations.
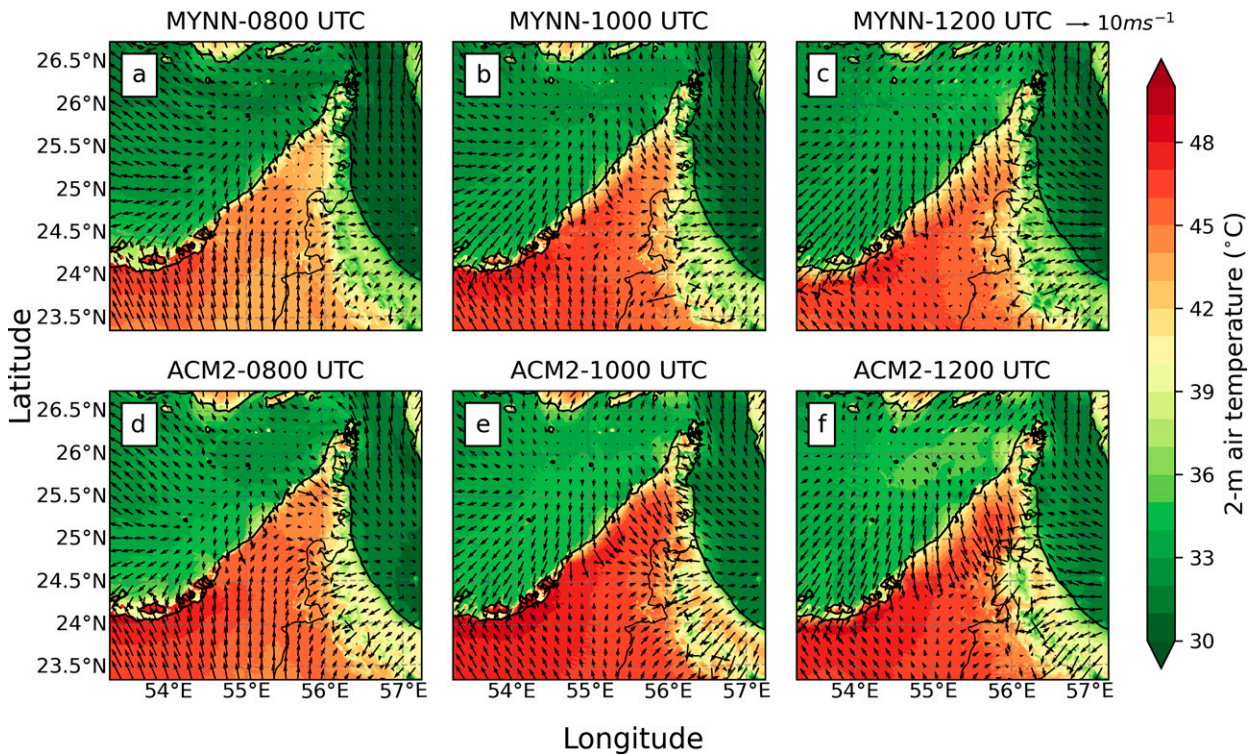
FIG. 8. WRF-simulated 2-m air temperature (shaded; °C) and 10-m wind field (vectors) from the (a)–(c) MYNN run and (d)–(f) ACM2 run valid at (left) 0800, (center) 1000, and (right) 1200 UTC 14 Jul 2015.

The maps of horizontal wind divergence and sea breeze in the MYNN and ACM2 simulations (not shown) indicate that these two simulations do not develop the major cold pool that converges with the sea breeze from the Arabian Gulf. For the same reason, these two model runs fail to simulate the band of convection on the west coast of the UAE, though these simulations show strong moisture transport from the Arabian Gulf (Figs. 8c,f).

5. Impact of the horizontal grid spacing

So far, we discussed results only from the 1-km domain. However, it is worth examining how well the model can reproduce the deep convection and precipitation pattern if we use a coarser horizontal grid spacing. Specifically, the development of the cold pool and its convergence with the sea breeze are the two aspects most worth exploring. Therefore, we perform two additional simulations, one with only the outermost 9-km domain and the other one with two nested domains of 9- and 3-km horizontal grid spacing. Both of these simulations use the QNSE PBL scheme. All the other settings are unchanged relative to the earlier set of simulations.

The top and middle rows in Fig. 10 show snapshots of the model-simulated column-maximum reflectivity. All three simulations show the development of convection along the Al Hajar Mountains at 0900 UTC. The structure of the convective band in all three runs is also similar, albeit the convection in the 9-km run is weaker than the convection in the other

two simulations. For instance, the 9-km simulation at 0900 UTC shows a maximum value of ~40 dBZ, whereas the other two runs indicate a maximum value of ~54 dBZ. The deep convection in the 1-km simulation also develops over a broader area.

At 1145 UTC, all simulations develop convection parallel to the west coast of the UAE. This convective band is a manifestation of the convergence between the sea breeze from the Arabian Gulf and the cold pools from neighboring convective activity. The model run reproduces this convective band even with a 9-km horizontal grid spacing (Fig. 10d), albeit much weaker in intensity and smaller in extent. The 3- and 1-km runs simulate the development of this convective band very well. However, there are noticeable differences between these two simulations in the locations of maximum reflectivity. The 1-km simulation indicates strong convection over a larger area than the convection in the 3-km simulation. A comparison with the observed radar reflectivity (Figs. 4a–c) reveals that the 1-km simulation is more consistent with the radar observations. Overall, there is an added value when using finer-resolution grids while simulating localized summertime convective systems over this portion of the Arabian Peninsula. The parent domain is capable of reproducing the underlying mechanisms leading to deep convection, but adding finer-resolution nests helps capture the intensity of the convection more realistically.

Figure 10 clearly shows that the development of secondary convection near the west coast of the UAE occurs in both of
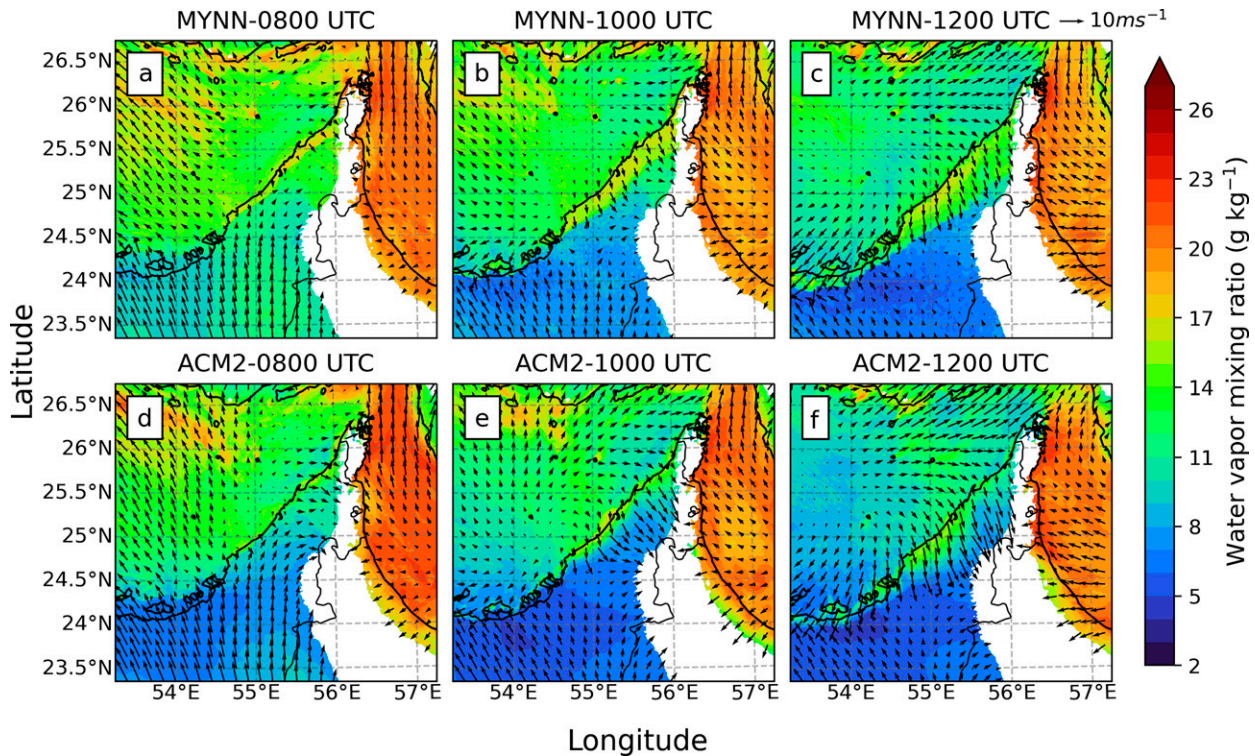
FIG. 9. As in Fig. 8, but for water vapor mixing ratio (shaded; g kg^{-1}) and wind field (vectors) at 975 hPa. The white color indicates terrain above the 975-hPa surface.

the lower resolution simulations (9- and 3-km) as well. Therefore, it is worth examining how well the model captures the cold pools at coarser horizontal grid spacing. Figure 11 illustrates the structure of cold pools from the 9- and 3-km runs. A comparison of the horizontal divergence fields (Fig. 11) with Figs. 7c and 7d, which show the corresponding fields from the 1-km simulation, suggests that the cold pool is notably weaker in lower resolution simulations, particularly in the 9-km simulation. However, there is no discernible difference in the strength of the sea breeze in lower-resolution runs. Since the intensity of cold pools and the diverging winds associated with the convective outflow is much weaker in 9- and 3-km simulations, the convergence pattern resulting from the convergence of the cold pools with the sea breeze is also weaker in lower-resolution runs. Figure 11 suggests that the weaker cold pool leads to a weaker convergence in the lower-resolution simulations, although a smaller grid size may yield larger divergence values in the 3- and 1-km runs.

We compare the time evolution of reflectivity and rainfall averaged over the domain to analyze how the time evolution of convection and precipitation varies with horizontal resolution. Figure 12a illustrates that the 9-km simulation develops convection approximately 1 h later than the 1-km simulation. The 3-km simulation also indicates a delay of almost 30 min relative to the convective development in the 1-km run. The delay in CI with coarser resolution models is documented in several previous studies (e.g., Petch et al. 2002; Paulius and Garner 2006; Hohenegger et al. 2015). The smoother topography in the

coarser resolution runs is also likely to delay CI. However, the temporal evolution of the spatial structure of deep convection reveals that although there is a delay in CI in the coarser resolution model runs, there is no discernible difference in the timing of further development, propagation, and dissipation (not shown). Therefore, although the 9-km model run shows a delay in CI, the northward and westward propagation of deep convection is much faster in the 9-km run. Figure 12b suggests that the delay in CI in the coarser resolution simulations is also reflected in the rainfall. While both 3- and 1-km runs show a uniform rainfall intensity throughout the period, the 9-km model run shows a single heavy episode of rainfall between 1030 and 1100 UTC. The 1- and 3-km model runs also produce approximately 75% and 50% more rainfall, respectively, than the 9-km model run.

To examine how horizontal grid spacing impacts the vertical motions, we perform isentropic analysis (analyzing motions on surfaces of constant entropy) here. Isentropic analysis takes advantage of the fact that equivalent potential temperature is quasi-conserved in convective motions, and therefore, one can track the vertical displacement of air parcels on constant entropy surfaces. One advantage of isentropic analysis is that it inherently filters out reversible motions such as gravity waves. Isentropic analysis helps us visualize the depth of convection and reveals the degree of mixing of air parcels in terms of θ_e. Therefore, by performing isentropic analysis for model output having different horizontal grid spacing, one can understand how the vertical extent of deep
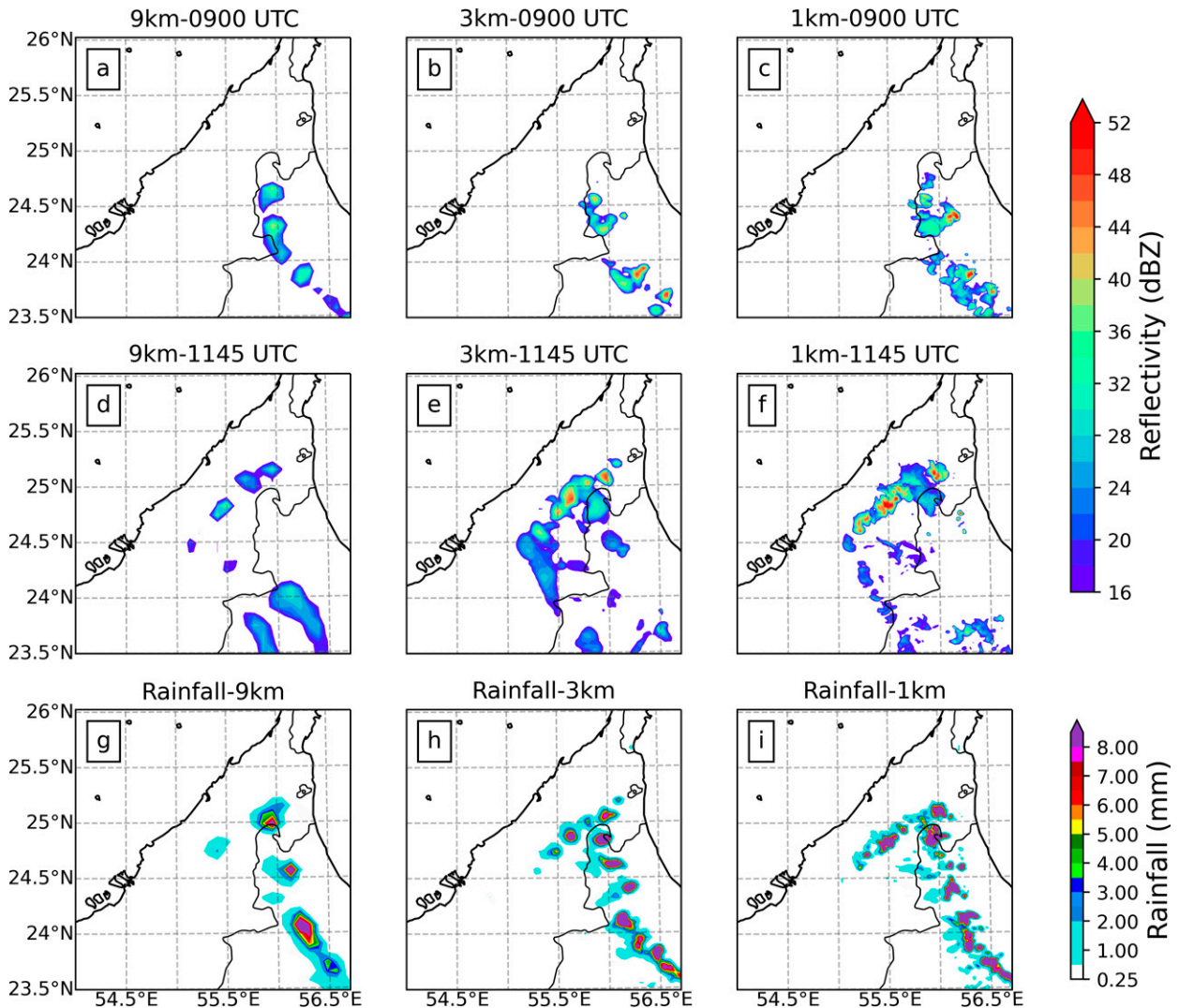
FIG. 10. The model-simulated column-maximum reflectivity at (a)–(c) 0900 UTC and (d)–(f) 1145 UTC from the (left) 9-km run; (center) 3-km run; and (right) 1-km run. Also shown is 24-h accumulated rainfall (valid at 0000 UTC 15 Jul 2015) from the (g) 9-, (h) 3-, and (i) 1-km runs.

convection and the entertainment varies with the model's horizontal grid size.

By reducing the four spatiotemporal coordinates to θ_e–p coordinates—θ_e and p are the equivalent potential temperature and pressure, respectively—one can visualize the irreversible overturning motions associated with the convection efficiently. The isentropic streamfunction ψ is defined as

$$\psi(p, \theta_{e0}) = \frac{1}{L_x L_y P} \int_0^P \int_0^{L_y} \int_0^{L_x} -\frac{\omega}{g} H[\theta_e(x, y, p, t) - \theta_{e0}] \, dx \, dy \, dt,$$
(1)

where L_x and L_y are the zonal and meridional extent of the domain, P is the averaging time period, and H is the Heaviside function: $H(x)$ is 1 for $x > 0$ and is 0 otherwise. Also, ω is pressure vertical velocity, g is acceleration due to gravity

(9.81 m s^{-2}), and θ_{e0} is an arbitrary constant value. Essentially, ψ accounts for the net vertical mass transport per unit area and time, at a given pressure level p, of all of the air parcels with an equivalent potential temperature less than θ_{e0}.

Figures 12c–e show the isentropic streamfunction computed for an area covering 54.5°–57.2°E and 23.4°–25.5°N for the period 0600–1400 UTC. The basic structure of the convective overturning circulation in all simulations is mostly similar, except that convection on finer grids reaches greater heights. The streamfunction pattern indicates very strong dry convection (dark red shading), which is associated with θ_e values around 340 K. Dry convection is characterized by minimal changes in θ_e values with height, as the intrusion of the ambient dry air does not change the θ_e values of convecting dry air parcels. Figures 12c–e indicate that the bulk of the convective overturning is due to the dry, inland convection, which is
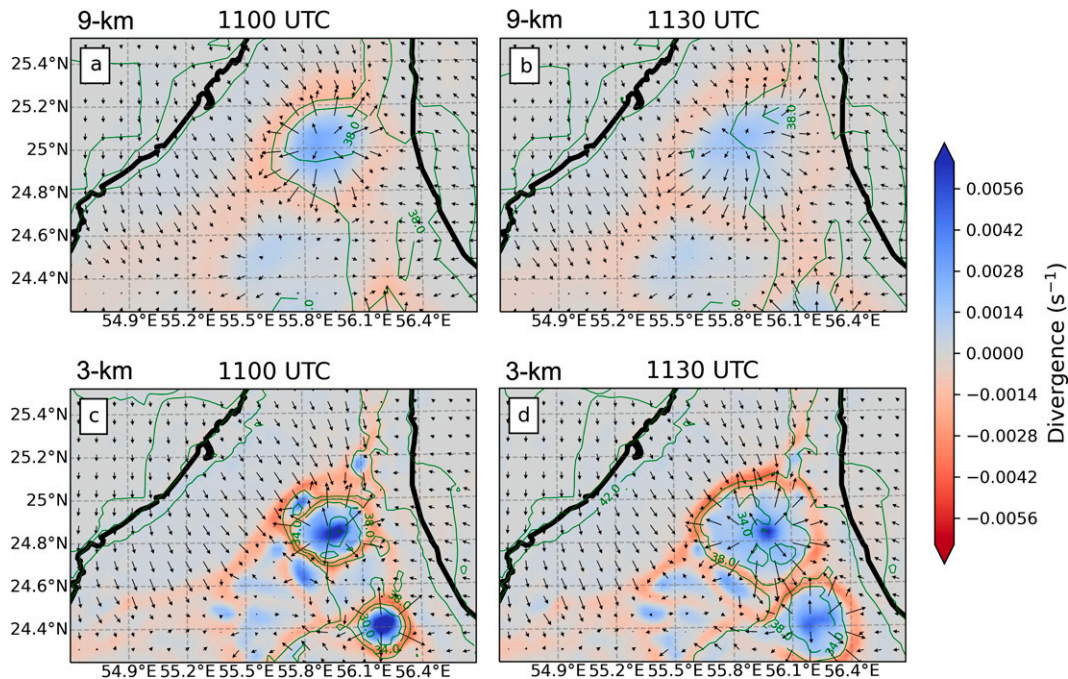
FIG. 11. Divergence of 10-m horizontal wind (shaded; s^{-1}) and 10-m horizontal wind (vectors) overlaid with 2-m temperature (green contours; °C) at (left) 1100 and (right) 1130 UTC from the (a),(b) 9- and (c),(d) 3-km runs. Thick black lines mark the coastline.

confined below ~450 hPa. All three simulations capture this dry convection reasonably well. The streamfunction pattern indicates the presence of air with very high values of θ_e (~375 K) in the lower troposphere, which is the moisture-rich air from the Gulf of Oman. This moist air undergoes ascending motion and reaches the upper troposphere. In the 9-km run, moist convection reaches up to 350-hPa (Fig. 12c), whereas in the 3- and 1-km runs, the moist convection reaches up to ~200- and ~150-hPa, respectively. The moist air mixes with dry inland air due to entertainment as the air parcels ascend. Therefore, moist convection is characterized by a decrease in θ_e values with height. Hence, the tilt in the pattern of streamfunction implies the degree of dry-air intrusion. The tilt in the streamfunction below 800-hPa is much greater for the 9-km run, whereas it is weakest for the 1-km run. The larger tilt in the 9-km run suggests that the 9-km simulation undergoes stronger entrainment, whereas dry-air intrusion is minimal for the 1-km simulation. As a result of this stronger mixing in the 9-km run, updrafts weaken and their equivalent potential temperatures drop below 350 K at 600 hPa. In contrast, the 3-km run and the 1-km run show that, with less entrainment, updrafts maintain an equivalent potential temperature above 350 K up to 300 hPa.

6. Summary and conclusions

The results from a cloud-resolving scale numerical simulation of a summertime convective system that occurred on 14 July 2015 over the Al Hajar Mountains and the UAE region are presented in this study. We used the WRF Model with a horizontal grid spacing of 1 km. To investigate the model's sensitivity to PBL parameterization schemes, we tested three different schemes: QNSE, MYNN, and ACM2.

The event consists of two major convective bands, one near the Al Hajar Mountains and another one parallel to the west coast of the UAE. The convection initially develops on the mountain peaks when the sea breeze from the Gulf of Oman encounters high terrain and the mean southerly and southwesterly flow over land. The moist convection then propagates southward and northwestward. A second prominent band of deep convection develops in the afternoon hours just inland from and parallel to the west coast of the UAE as a manifestation of the convergence between the cold pools and the sea breeze from the Arabian Gulf. The results show that the simulation using the QNSE PBL scheme captures the entire sequence of events, including the convection initiation over the Al Hajar Mountains and subsequent northwestward propagation of the convective activity quite well. The model simulation generally indicates higher rainfall amounts than observed, which could be partly due to the uncertainties in radar observations over complex terrain. The QNSE run produces a larger land–sea temperature contrast and a stronger sea breeze than the other two simulations. It also produces a stronger wind field over land, which is crucial in developing convergence that supports the deep convection near the mountains. The MYNN run simulates colder 2-m temperatures and a weaker sea breeze, and the ACM2 run simulates a relatively drier lower troposphere over land. Therefore, the MYNN and ACM2 simulations fail to reproduce the moisture transport effectively. Nevertheless, these two simulations show the convective initiation and further development of moist convection near the
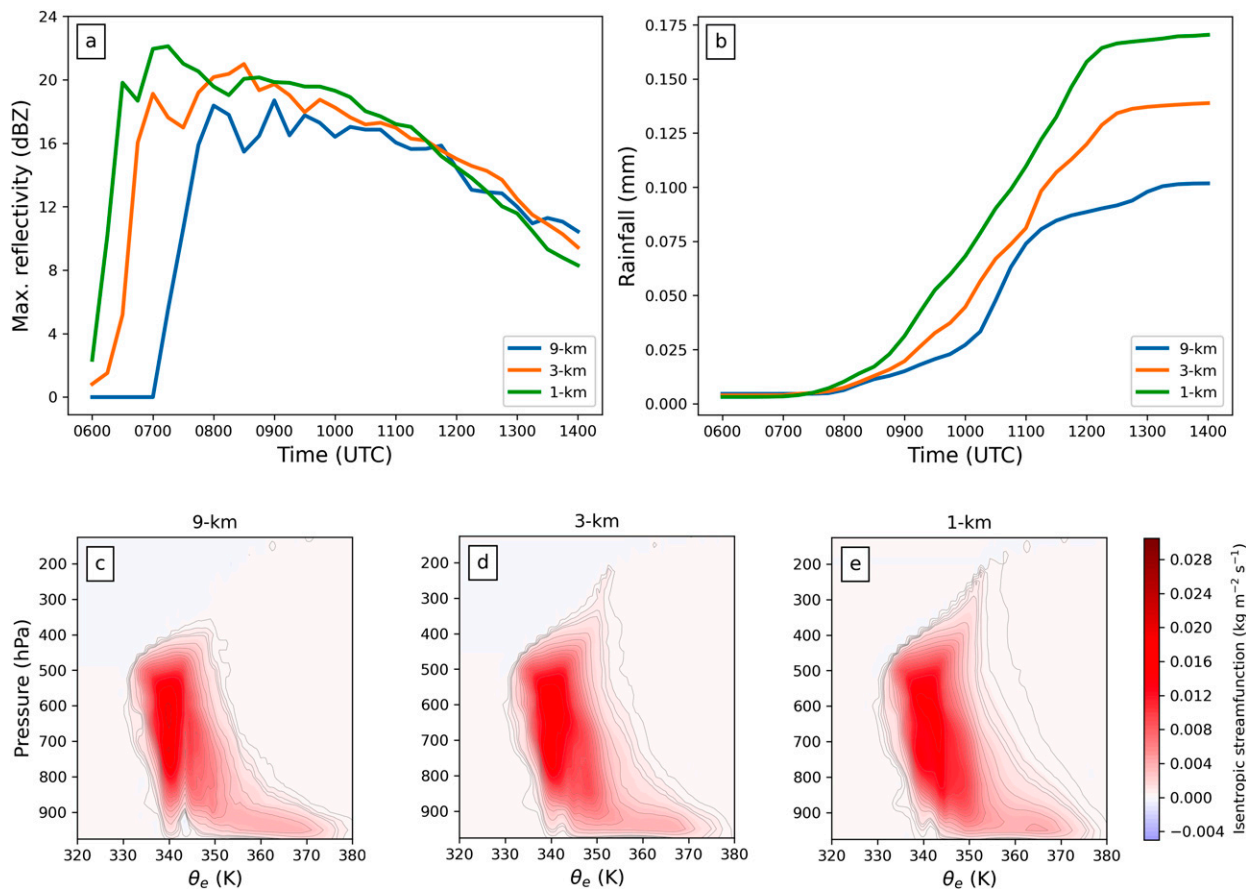
FIG. 12. Time series of (a) domain-averaged column-maximum reflectivity and (b) domain-averaged accumulated precipitation from the resolution sensitivity experiments. Also shown are the isentropic streamfunction computed from the (c) 9-, (d) 3-, and (e) 1-km model runs.

Al Hajar Mountains to an extent, with a more scattered structure in the MYNN run. However, the northward propagation of convection is absent in both the MYNN and ACM2 runs, and these simulations fail to develop a major convective plume west of the mountains. Cold pools from this particular convective plume converge with the sea breeze from the Arabian Gulf. While the QNSE run realistically simulates the development of the cold pool and subsequent convergence with the sea breeze, the other two simulations miss these events entirely. A recent study by Schwitalla et al. (2020), which investigated the simulation of the same convective event as the current study, observed poor skill in the rainfall simulation with the MYNN and YSU PBL schemes, whereas our study suggests a remarkable improvement in the rainfall simulation with the use of the QNSE PBL scheme. Future studies, therefore, may focus on testing the robustness of the QNSE PBL parameterization scheme for the simulation of several summertime convective events.

We performed another set of experiments to examine the skill of the WRF Model with coarser horizontal grid spacing (9- and 3-km) in reproducing the moist convection and the convergence of cold pools with the sea breeze. A comparison with the radar observations reveals that the 1-km model run shows better skill in reproducing the spatial structure of

convective bands. However, the 3-km run also simulates the convective event reasonably well, including the secondary development of convection near the west coast of the UAE. A detailed examination of the convergence of the cold pools and the sea breeze at different horizontal grid spacings reveals that cold pools and the divergence are considerably stronger in the high-resolution runs, though there is no discernible difference in the strength of the sea breeze. Therefore, the weaker cold pool leads to weaker convergence in the lower-resolution model runs. The time evolution of domain-averaged simulated radar reflectivity suggests that CI occurs earliest in the 1-km run, followed by the initiation in the 3-km model run about 30 min later and the 9-km model run almost 1 h later. Isentropic analysis indicates that the convection in the 1-km simulation reaches a greater height than in the other two simulations. Overall, the results from this experiment indicate that the broader structure of the deep convection develops in the 9-km run also, although at a lower intensity. The choice of the PBL parameterization scheme, through its effect on representing the sea breeze, has a more significant impact on convection than the horizontal resolution of the model.

The results from this study are particularly important because no study is available in the literature that demonstrates

the sequence of events involved in the summertime convective events over the Al Hajar Mountains and adjoining areas of the UAE. Moreover, a couple of previous studies that attempted to simulate similar convective events reported relatively poor skill in reproducing the observed rainfall pattern (Schwitalla et al. 2020; Francis et al. 2021). Therefore, our study provides significant value in terms of realistic simulation of the entire sequence of events associated with the summertime convective event discussed here. The present model configuration appears promising, and therefore it possibly can be utilized in the ongoing cloud-seeding experiments to identify CI in advance, after testing on more cases.

Data availability statement. Access to the observational datasets presented here is restricted, and the readers should request them from NCM, Abu Dhabi. The WRF Model output can be made available upon request to NYUAD. The ERA5 dataset is available online (https://cds.climate.copernicus.eu/).

REFERENCES

Ackerman, S. A., and S. K. Cox, 1982: The Saudi Arabian heat low: Aerosol distributions and thermodynamic structure. *J. Geophys. Res.*, **87**, 8991–9002, https://doi.org/10.1029/JC087iC11p08991.

Al Hosari, T., and Coauthors, 2021: The UAE cloud seeding program: A statistical and physical evaluation. *Atmosphere*, **12**, 1013, https://doi.org/10.3390/atmos12081013.

Aldababseh, A., M. Temimi, P. Maghelal, O. Branch, and V. Wulfmeyer, 2018: Multi-criteria evaluation of irrigated agriculture suitability to achieve food security in an arid environment. *Sustainability*, **10**, 803, https://doi.org/10.3390/su10030803.

Branch, O., A. Behrendt, Z. Gong, T. Schwitalla, and V. Wulfmeyer, 2020: Convection initiation over the eastern Arabian Peninsula. *Meteor. Z.*, **29**, 67–77, https://doi.org/10.1127/metz/2019/0997.

Bruintjes, R., and D. Yates, 2003: Report on review and assessment of the potential for cloud seeding to enhance rain-fall in the Sultanate of Oman. NCAR Rep.

Chen, X., O. M. Pauluis, and F. Zhang, 2018: Regional simulation of Indian summer monsoon intraseasonal oscillations at gray-zone resolution. *Atmos. Chem. Phys.*, **18**, 1003–1022, https://doi.org/10.5194/acp-18-1003-2018.

Fonseca, R., D. Francis, N. Nelli, and M. Thota, 2022: Climatology of the heat low and the intertropical discontinuity in the Arabian Peninsula. *Int. J. Climatol.*, **42**, 1092–1117, https://doi.org/10.1002/joc.7291.

Francis, D., N. Alshamsi, J. Cuesta, A. Gokcen Isik, and C. Dundar, 2019: Cyclogenesis and density currents in the Middle East and the associated dust activity in September 2015. *Geosciences*, **9**, 376, https://doi.org/10.3390/geosciences9090376.

——, M. Temimi, R. Fonseca, N. R. Nelli, R. Abida, M. Weston, and Y. Whebe, 2021: On the analysis of a summertime convective event in a hyperarid environment. *Quart. J. Roy. Meteor. Soc.*, **147**, 501–525, https://doi.org/10.1002/qj.3930.

Hersbach, H., and Coauthors, 2020: The ERA5 global reanalysis. *Quart. J. Roy. Meteor. Soc.*, **146**, 1999–2049, https://doi.org/10.1002/qj.3803.

Hohenegger, C., L. Schlemmer, and L. Silvers, 2015: Coupling of convection and circulation at various resolutions. *Tellus*, **67A**, 26678, https://doi.org/10.3402/tellusa.v67.26678.

Iacono, M. J., J. S. Delamere, E. J. Mlawer, M. W. Shephard, S. A. Clough, and W. D. Collins, 2008: Radiative forcing by long-lived greenhouse gases: Calculations with the AER radiative transfer models. *J. Geophys. Res.*, **113**, D13103, https://doi.org/10.1029/2008JD009944.

Jing, X., and Coauthors, 2020: Convection-permitting regional climate simulations in the Arabian Gulf region using WRF driven by bias-corrected GCM data. *J. Climate*, **33**, 7787–7815, https://doi.org/10.1175/JCLI-D-20-0155.1.

Knippertz, P., and Coauthors, 2009: Dust mobilization and transport in the northern Sahara during SAMUM 2006—A meteorological overview. *Tellus*, **61B**, 12–31, https://doi.org/10.1111/j.1600-0889.2008.00380.x.

Murad, A. A., H. Al Nuaimi, and M. Al Hammadi, 2007: Comprehensive assessment of water resources in the United Arab Emirates (UAE). *Water Resour. Manage.*, **21**, 1449–1463, https://doi.org/10.1007/s11269-006-9093-4.

Nakanishi, M., and H. Niino, 2006: An improved Mellor-Yamada level-3 model: Its numerical stability and application to a regional prediction of advection fog. *Bound.-Layer Meteor.*, **119**, 397–407, https://doi.org/10.1007/s10546-005-9030-8.

——, and ——, 2009: Development of an improved turbulence closure model for the atmospheric boundary layer. *J. Meteor. Soc. Japan*, **87**, 895–912, https://doi.org/10.2151/jmsj.87.895.

Niu, G.-Y., and Coauthors, 2011: The community Noah land surface model with multiparameterization options (Noah-MP): 1. Model description and evaluation with local-scale measurements. *J. Geophys. Res.*, **116**, D12109, https://doi.org/10.1029/2010JD015139.

Odhiambo, G. O., 2017: Water scarcity in the Arabian Peninsula and socio-economic implications. *Appl. Water Sci.*, **7**, 2479–2492, https://doi.org/10.1007/s13201-016-0440-1.

Ouarda, T. B., C. Charron, K. N. Kumar, P. R. Marpu, H. Ghedira, A. Molini, and I. Khayal, 2014: Evolution of the rainfall regime in the United Arab Emirates. *J. Hydrol.*, **514**, 258–270, https://doi.org/10.1016/j.jhydrol.2014.04.032.

Pauluis, O., and S. Garner, 2006: Sensitivity of radiative–convective equilibrium simulations to horizontal resolution. *J. Atmos. Sci.*, **63**, 1910–1923, https://doi.org/10.1175/JAS3705.1.

Petch, J., A. Brown, and M. Gray, 2002: The impact of horizontal resolution on the simulations of convective development over land. *Quart. J. Roy. Meteor. Soc.*, **128**, 2031–2044, https://doi.org/10.1256/003590002320603511.

Pleim, J. E., 2007a: A combined local and nonlocal closure model for the atmospheric boundary layer. Part I: Model description and testing. *J. Appl. Meteor. Climatol.*, **46**, 1383–1395, https://doi.org/10.1175/JAM2539.1.

——, 2007b: A combined local and nonlocal closure model for the atmospheric boundary layer. Part II: Application and evaluation in a mesoscale meteorological model. *J. Appl. Meteor. Climatol.*, **46**, 1396–1409, https://doi.org/10.1175/JAM2534.1.

Schwitalla, T., O. Branch, and V. Wulfmeyer, 2020: Sensitivity study of the planetary boundary layer and microphysical schemes to the initialization of convection over the Arabian Peninsula. *Quart. J. Roy. Meteor. Soc.*, **146**, 846–869, https://doi.org/10.1002/qj.3711.

Skamarock, W. C., and Coauthors, 2019: A description of the Advanced Research WRF Model version 4. NCAR Tech. Note NCAR/TN-556+STR, 145 pp., https://doi.org/10.5065/1dfh-6p97.

Smith, E. A., 1986: The structure of the Arabian heat low. Part I: Surface energy budget. *Mon. Wea. Rev.*, **114**, 1067–1083, https://doi.org/10.1175/1520-0493(1986)114<1067:TSOTAH>2.0.CO;2.

Steinhoff, D. F., R. Bruintjes, J. Hacker, T. Keller, C. Williams, T. Jensen, A. Al Mandous, and O. A. Al Yazeedi, 2018: Influences of the monsoon trough and Arabian heat low on summer rainfall over the United Arab Emirates. *Mon. Wea. Rev.*, **146**, 1383–1403, https://doi.org/10.1175/MWR-D-17-0296.1.

Sukoriansky, S., B. Galperin, and V. Perov, 2005: Application of a new spectral theory of stably stratified turbulence to the atmospheric boundary layer over sea ice. *Bound.-Layer Meteor.*, **117**, 231–257, https://doi.org/10.1007/s10546-004-6848-4.

Taraphdar, S., and Coauthors, 2021: WRF gray-zone simulations of precipitation over the Middle-East and the UAE: Impacts of physical parameterizations and resolution. *J. Geophys. Res. Atmos.*, **126**, e2021JD034648, https://doi.org/10.1029/2021JD034648.

Temimi, M., and Coauthors, 2020: Assessing the impact of changes in land surface conditions on WRF predictions in arid regions. *J. Hydrometeor.*, **21**, 2829–2853, https://doi.org/10.1175/JHM-D-20-0083.1.

Thompson, G., and T. Eidhammer, 2014: A study of aerosol impacts on clouds and precipitation development in a large winter cyclone. *J. Atmos. Sci.*, **71**, 3636–3658, https://doi.org/10.1175/JAS-D-13-0305.1.

Wehbe, Y., and M. Temimi, 2021: A remote sensing-based assessment of water resources in the Arabian Peninsula. *Remote Sens.*, **13**, 247, https://doi.org/10.3390/rs13020247.

——, D. Ghebreyesus, M. Temimi, A. Milewski, and A. Al Mandous, 2017: Assessment of the consistency among global precipitation products over the United Arab Emirates. *J. Hydrol.*, **12**, 122–135, https://doi.org/10.1016/j.ejrh.2017.05.002.

——, M. Temimi, D. T. Ghebreyesus, A. Milewski, H. Norouzi, and E. Ibrahim, 2018: Consistency of precipitation products over the Arabian Peninsula and interactions with soil moisture and water storage. *Hydrol. Sci. J.*, **63**, 408–425, https://doi.org/10.1080/02626667.2018.1431647.

——, and Coauthors, 2019: Analysis of an extreme weather event in a hyper-arid region using WRF-hydro coupling, station, and satellite data. *Nat. Hazards Earth Syst. Sci.*, **19**, 1129–1149, https://doi.org/10.5194/nhess-19-1129-2019.

——, M. Temimi, and R. F. Adler, 2020: Enhancing precipitation estimates through the fusion of weather radar, satellite retrievals, and surface parameters. *Remote Sens.*, **12**, 1342, https://doi.org/10.3390/rs12081342.

——, and Coauthors, 2021: Analysis of aerosol–cloud interactions and their implications for precipitation formation using aircraft observations over the United Arab Emirates. *Atmos. Chem. Phys.*, **21**, 12 543–12 560, https://doi.org/10.5194/acp-21-12543-2021.

Weston, M., N. Chaouch, V. Valappil, M. Temimi, M. Ek, and W. Zheng, 2019: Assessment of the sensitivity to the thermal roughness length in Noah and Noah-MP land surface model using WRF in an arid region. *Pure Appl. Geophys.*, **176**, 2121–2137, https://doi.org/10.1007/s00024-018-1901-2.